processes

MDPI

Article

Computational Fluid Dynamics Modeling of Multiphase Flows in a Side-Blown Furnace: Effects of Air Injection and Nozzle Submerged Depth

Peng Long [1,2], Zhuo Chen [1] and Yan-Po Song [1,*]

[1] School of Energy Science and Engineering, Central South University, Changsha 410083, China; longpeng@guat.edu.cn (P.L.); chenzhuo@csu.edu.cn (Z.C.)
[2] School of Energy and Building Environment, Guilin University of Aerospace Technology, Guilin 541004, China
* Correspondence: songyanpo@csu.edu.cn; Tel.: +86-1-387-311-7679

Abstract: The side-blown smelting process is becoming popular in the modern metallurgical industry due to its large potential for dealing with complex materials. To further enhance its efficiency, it is essential to comprehensively understand the complex gas–liquid flow behavior in the smelting bath. In this study, the volume-of-fluid method is employed to establish computational fluid dynamics modeling on a 1:5 scaled model of a side-blown furnace. The simulation was validated against the experimental results. Notably, the influences of the nozzle's submerged depth, injection velocity, and angle were systematically investigated. The results show that increasing the injection velocity from 29.44 to 58.88 m/s resulted in 52.97%, 116.67%, 500.00%, and 5.88% increases in the interface area, liquid velocity, liquid turbulent kinetic energy, and gas penetration depth, respectively. The maximum gas–liquid interface area, gas penetration depth, velocity, and turbulence of the liquid were found at an injection angle of 30°. Furthermore, increasing the submerged depth increased the interface area and the velocity of the liquid but decreased the turbulent kinetic energy of the liquid. Overall, increasing the injection velocity is considered a more effective measure to strengthen the smelting intensity.

Keywords: multiphase flow; side-blown smelting furnace; injection velocity; injection angle; nozzle submerged depth

check for updates

Citation: Long, P.; Chen, Z.; Song, Y.-P. Computational Fluid Dynamics Modeling of Multiphase Flows in a Side-Blown Furnace: Effects of Air Injection and Nozzle Submerged Depth. *Processes* **2024**, *12*, 1373. https://doi.org/10.3390/pr12071373

Academic Editor: Jiaqiang E

Received: 4 June 2024
Revised: 27 June 2024
Accepted: 27 June 2024
Published: 1 July 2024

1. Introduction

Bath smelting is one of the main technologies for copper pyrometallurgical production. According to the location where the air is injected into the furnace, it is usually divided into three types: bottom-blown, side-blown, and top-blown. Side-blown smelting is the most widely adopted in modern industries because of its excellent adaptability to various materials and economic advantages, such as low construction investment, a short construction period, and low operating costs. Generally, when the oxygen-enriched airflow is injected into the bath, it experiences dispersion, aggregation, and breakup. The bubble motion causes the slag and melt to flow, tumble, and splash. These complex behaviors of gaseous and melt phases directly relate to the smelting efficiency. However, due to the high temperature and tight environment, it is difficult to directly conduct industrial experiments in the side-blown bath. Alternatively, hydraulic experiments and computational fluid dynamics (CFD) modeling are considered more effective to explore the mechanism and characteristics of this complex process.

Researchers have conducted numerous model experiments on gas–liquid flows in bath smelting [1]. Oryall et al. [2] used high-speed cameras to study the distribution of gas fraction and bubble frequency within the submerged jet under isothermal and nonreactive conditions for various nozzle diameters and jet Froude numbers. Ternstedt et al. [3]

studied the mixing time in a side-blown converter by measuring the conductivity in the water bath using KCl as a tracer. By establishing a one-fifth-scale physical slice model of a bottom-blown furnace and applying Particle Image Velocimetry (PIV), Wang et al. [4] measured the flow field at various pool depths, nozzle installation angles, and gas flow rates. Zhang et al. [5] studied the liquid reaction in a submerged top-blow agitation process by using planar laser-induced fluorescence (PLIF) technology based on the principle of fluorescence quenching. Akashi et al. [6] performed an experimental investigation of the top-blowing process. They employed visualization techniques by injecting the inert gas argon into a GaInSn liquid metal and combined X-ray radiography with high-speed imaging technology. Bubble motion is investigated by taking images with high-speed cameras in the experiments; the mixing time of the melting bath is estimated by measuring the conductivity via conductivity probes; and the flow field/pattern is reconstructed using PIV, PLIF, or X-ray imaging of the melt. One of the represent limitations of hydraulic experiments is that only specific parameters can be considered in physical constructions. Once the reactor structure or blowing pattern changes, the results and equations obtained may not be further applicable. Moreover, it is currently challenging to obtain accurate 3D flow information in experiments, such as bubble aggregation and fragmentation processes, bubble size distribution, turbulent pulsations, etc.

In contrast, CFD modeling has significant advantages in presenting detailed information on the transfer processes and chemical reactions of the two-phase system [7]. Research on gas–liquid two-phase systems is very extensive, involving research on multiple scales [8]. The mathematical models mostly use the volume-of-fluid (VOF) model, the level set model, or the coupled level set and volume-of-fluid (CLSVOF) model [9].

The numerical research carried out on the side-blown process covers a wide range of reactors, including Peirce–Smith (P-S) converters, Teniente, Vanyukov furnaces, oxygen-rich side-blown furnaces, etc. These reported studies provide a solid basis for the CFD modeling of side-blown smelting. Chibwe et al. [10,11] conducted a series of CFD simulations of a P-S converter using the VOF model and the realizable k-ε turbulence model. The mixing conditions at flow rates ranging from 0.00875 m^3/s to 0.01375 m^3/s were analyzed. It was found that the numerical results could well predict the mixing and dispersion characteristics in the converting bath. The dispersion of the matte in the slag phase increased with the airflow rate, whereas the dispersion of the slag phase in the matte was observed to decrease with the airflow rate. Valencia et al. [12] conducted a numerical study of a Teniente copper converter that combined both side-blown and bottom-blown gas injection. The gas–liquid system in the furnace was simulated using the VOF method and the standard k-ε turbulence models. The gas–liquid two-phase system was studied for bottom-blowing at three different Froude numbers (0, 36, and 64). The study revealed that gas injections through both the bottom and the side could effectively enhance fluid mixing without significantly increasing surface kinetic energy, thereby considerably improving the converter's conversion potential. Zhang et al. [13] conducted a numerical simulation of a multiphase flow in a Vanyukov furnace using the VOF method and the standard k-ε turbulence model. The research findings demonstrated that the numerical model was capable of predicting phase distribution, velocity distribution, and the relationship between the gas flow rate and slag velocity. The dominant frequency of the density signal over time was 0.29 Hz. As the inlet air velocity varied from 70 to 160 m/s, the peak mean velocity of the liquid increased from 2.17 to 4.99 m/s. Liu et al. [14] established a simulation of the two-phase flow in an oxygen-rich side-blown furnace, confirming that the realizable k-ε turbulence model could give a more accurate prediction of the flow patterns. Xiao et al. [15] adopted the VOF method and the realizable k-ε turbulence model in the simulation of the gas–slag–matte three-phase flow in an oxygen-rich side-blown copper smelting furnace. They divided the flow field in the furnace into five zones: the high-speed injection zone, the strong-loop zone, the weak-loop zone, the gas overflow separation zone, and the settling zone. The gas flow in the furnace was determined to be a periodic bubbly flow, with an average penetration depth of about 0.365 m and an injection period of about 1.251 s. Bian et al. [16,17] investigated the impact of the appropriate primary air injection mode on gas–liquid multiphase flow in the oxygen-rich side-blown bath smelting furnace, and they optimized the parameters through orthogonal test design. The findings revealed the order of influence on the smelting process and identified the optimal conditions, leading to a 45% improvement in smelting efficiency. Moreover, physical model experiments confirmed that the optimal conditions effectively enhanced the smelting efficiency of the furnace. Zou et al. [18] investigated the splashing behavior of melt in an oxygen-enriched side-blown furnace. The study found that as the airflow velocity increased, the height of the splashing gradually increased, reaching an average height of 1.01 m when the airflow velocity was 160 m/s. The height of the splashing decreased with an increase in the nozzle immersion depth. Raising the liquid level was beneficial in reducing the height of the splashing. In summary, these validated models and compared experiments inspired further research on the side-blown bath. However, few studies have investigated the effects on the interface area between phases and the kinematic characteristics of the two-phase system over time.

This study aims to investigate the gas–liquid two-phase flow characteristics over time in the side-blown bath, facilitating the understanding of complex flow phenomena and providing practical measures for strengthening the smelting intensity. To achieve this goal, the effects of air injection velocity, injection angle, and submerged depth were systematically investigated through numerical simulations. The numerical results were validated against experiments first to ensure the models' accuracy. Then, the multiphase flow behaviors were analyzed thoroughly, focusing on the gas–liquid interface area, turbulent kinetic energy, and airflow penetration depth. Overall, this study contributes valuable knowledge on the multiphase flow dynamics of side-blown bath smelting and provides practical measures to improve the furnace structure and operational model.

2. Model Building

2.1. Physical Development

Figure 1 depicts the structure of a side-blown smelting furnace located in China. During production, materials including copper concentrate and flux are fed into the bath through the concentrate inlet. Oxygen-enriched air is injected into the melt layer from the primary tuyere, creating intense agitation. This agitation facilitates the heat and mass transfer between slag and oxygen, accompanied by a series of chemical reactions. The secondary air enters the furnace through the flue area to oxidize any sulfur that has not yet reacted sufficiently, and all gases are ultimately discharged into a residual heat boiler from the flue.

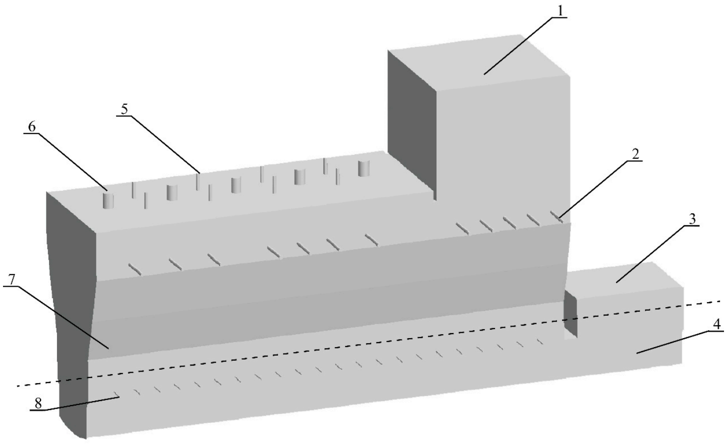

Figure 1. The side-blown furnace structure schematic diagram. 1. Outlet for flue gases; 2. secondary tuyere; 3. slag chamber; 4. melting bath; 5. secondary air inlet at the top; 6. concentrate inlet; 7. gas phase space; 8. primary tuyere.

To save the computational resources, based on the periodic structure, a slice model with only one pair of primary tuyeres was selected to make the simplification. The study mainly focuses on the characteristics of the gas–liquid two-phase system motion in the melting bath, without considering the influence of the inlet of secondary air from above. Therefore, a scaled-down model of the oxygen-rich side-blown furnace was created at a scale of 1:5, as shown in Figure 2.

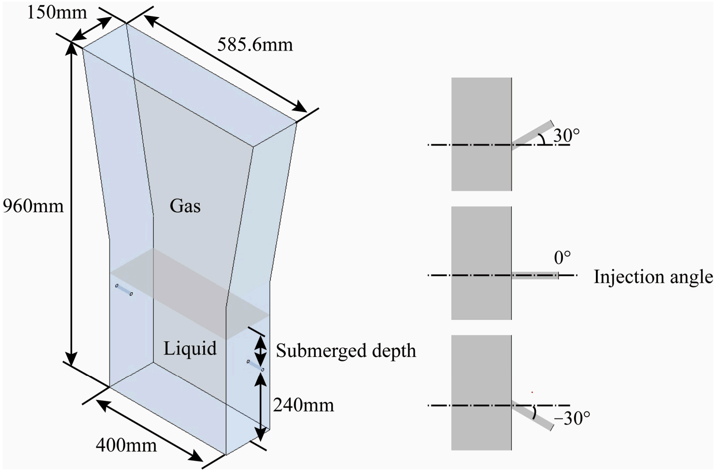

Figure 2. Schematic diagram of the structure of the scaled-down model.

The width of the model at the bottom is 400 mm, the width at the top is 585.6 mm, the thickness is 150 mm, the height of the model is 960 mm, the height of the nozzle from the bottom is 240 mm, the diameter of the nozzle is 8 mm, and the angle of the nozzle from the horizontal direction is $-30°$, $0°$, and $30°$. The submerged depth is the distance measured from the still-liquid surface to the nozzle's centerline.

2.2. Mathematical Model

The smelting process in a side-blown bath is a typical gas–liquid two-phase system with interaction and reaction processes. The VOF model based on the Eulerian method is suitable for stratified and free surface flows and can capture the two-phase interface very well. To analyze the phenomena such as the rise and breakup of the gas in the melting bath, as well as the tumbling and spattering of the melt, the VOF model was chosen in this study to simulate the motion behaviors of the gas and liquid phases in the model.

2.2.1. VOF Model

Since the effect of temperature is not considered in the numerical calculations, the system of equations mainly consists of continuity and momentum equations.

(1) Volume fraction continuity equation

The VOF model enables the tracing of interfaces between different phases by solving the continuity equation for the volume fraction of single or multiphase (other than the main phase), as shown in the expression in Equation (1) [19].

$$\frac{1}{\rho_q}\left[\frac{\partial}{\partial t}\left(\alpha_q\rho_q\right)+\nabla\cdot\left(\alpha_q\rho_q\vec{u}_q\right)\right]=0 \tag{1}$$

where the volume fraction of the main phase satisfies the following conditions:

$$\sum_{q=1}^{n}\alpha_q=1 \tag{2}$$

where: p and p_q are the density of the mixture and the qth phase, respectively, $\mathrm{kg/m^3}$; $\vec{u}$ is the velocity of the mixture, $\mathrm{m/s}$; α_q is the volume fraction of the qth phase in the mixture;

t is time, s; n is the number of all phases, which means a two-phase flow when n = 2; $\vec{u}_q$ is the velocity of the qth phase, m/s.

(2) Momentum equation

The conservation of momentum equation is a specific application of Newton's second law in fluid mechanics, which establishes the relationship between fluid density, velocity, pressure, and external forces. The equation is shown as Equation (3).

$$\frac{\partial}{\partial t}\left(\rho\vec{u}\right)+\nabla\cdot\left(\rho\vec{u}\vec{u}\right)=-\nabla p+\nabla\cdot\left[\mu\left(\nabla\vec{u}+\nabla\vec{u}^{T}\right)\right]+\rho\vec{g}+\vec{F} \tag{3}$$

in which:

$$\rho=\alpha_q\rho_q+\left(1-\alpha_q\right)\rho_p \tag{4}$$

$$\mu=\alpha_q\mu_q+\left(1-\alpha_q\right)\mu_p \tag{5}$$

where: p_q and p_p are the densities of the q phase and the p phase, respectively, kg/m^3; μ_q and μ_q are the kinematic viscosity of the q phase and p phase, respectively, Pa·s; $\vec{u}$ is the velocity of the mixed phase, m/s; p is the static pressure, Pa; $\vec{g}$ is the acceleration of gravity, m/s^2; $\vec{F}$ is the external body force (such as lift force, custom source term, etc.), N.

2.2.2. Turbulence Model

It was found that the results of the flow field are more consistent with the experiments when using the realizable k-ε turbulence model [14]. Therefore, the realizable k-ε turbulence model is used in this numerical study. The governing equations in the realizable k-ε turbulence model include the equation of the turbulent kinetic energy (k) and the turbulent energy dissipation rate (ε), as shown in Equations (6) and (7), respectively.

(1) k equation:

$$\frac{\partial}{\partial t}(\rho k)+\nabla\left(\rho\vec{u}k-\left(\mu+\frac{\mu_t}{\sigma_k}\right)\nabla k\right)=G_k-\rho\varepsilon \tag{6}$$

(2) ε equation:

$$\frac{\partial}{\partial t}(\rho\varepsilon)+\nabla\left(\rho\vec{u}\varepsilon-\left(\mu+\frac{\mu_t}{\sigma_\varepsilon}\right)\nabla\varepsilon\right)=\rho C_1 S\varepsilon-\rho C_2\frac{\varepsilon^2}{k+\sqrt{v\varepsilon}} \tag{7}$$

in which:

$$\mu_t=\frac{\rho C_\mu k^2}{\varepsilon},\ C_1=\max\left[0.43,\frac{\eta}{\eta+5}\right],\ \eta=S\frac{k}{\varepsilon},\ S=\sqrt{2S_{ij}S_{ij}} \tag{8}$$

where S is the modulus of the mean strain rate tensor; G_k is the turbulent kinetic energy due to the mean velocity gradient, $C_2=1.9$, $\sigma_k=1.0$, $\sigma_\varepsilon=1.2$.

2.3. Boundary Conditions and Calculation Methods

The simulation calculations were performed using the Fluent 2022R1, a software developed by ANSYS, Inc., a company located in Pittsburgh, PA, USA. The boundary conditions of the side-blown nozzle in the computational domain were set to the velocity inlet, the outlet in the top position was set to the pressure outlet, and all the walls were set as non-slip walls. The PISO algorithm was selected for the pressure–velocity coupling scheme, and the time step was set to 10^{-4} s.

During the gas–liquid two-phase flow of the side-blown process, the gas and liquid are mainly affected by inertia and gravity. Under the same modified Froude number, the relative influence of inertia and gravity is similar. Based on the modified Froude number criterion relationship, by analyzing and comparing the behavior laws of fluid motion in the model under different operating parameters, the laws of different fluid behaviors in the prototype oxygen-enriched side-blown furnace can be inferred. The gas injection velocity of the prototype oxygen-enriched side-blown furnace varies from 120 m/s to 250 m/s, the copper slag density is 4003 kg/m^3, and the mixed gas density entering the furnace is 1.401 kg/m^3. In the CFD simulations, the liquid is water with a density of 998 kg/m^3, and the air density is 1.293 kg/m^3. Therefore, according to the modified Froude number criterion (Equation (9)), the gas injection velocity of the model varies between 29 m/s and 60 m/s during numerical calculations.

$$Fr' = \frac{\rho_g u^2}{\text{gd}(\rho_l - \rho_g)} \tag{9}$$

2.4. Grid Independence Test and Model Validation

The mesh is structured with local refinement at the nozzle region to obtain geometries with mesh numbers 183,788, 415,424, and 704,786, respectively. At an injection velocity of 29.44 m/s, an injection angle of 0°, and a submerged depth of 100 mm, the average velocity versus time curves in the liquid-phase region for different numbers of grid cells are shown in Figure 3. The results of medium and fine grids are similar, and the variation trend is the same, while the coarse grid shows deviation, and the velocity fluctuates more. The average velocity in the liquid-phase region for the three grid sizes is shown in Table 1. The average velocity of the fluid in the coarse grid is smaller, while the average velocity of the fluid in the medium and fine grids is almost equal. Considering the computational resources and time duration, the mesh number level of 415,424 is selected as the benchmark for the calculation. At the same time, the nozzle angles of −30° and 30° have mesh numbers 422,790 and 423,084, respectively, when the nozzle angle is changed.

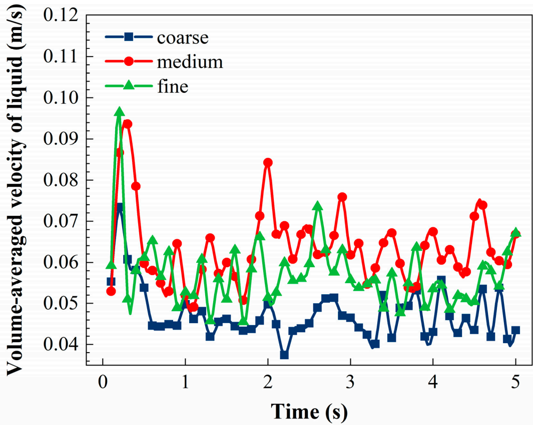

Figure 3. The curve of the velocity of the liquid varies with time under different meshes.

Table 1. Mesh independence validation.

Physical Quantity	**Number of Grids (Simulation Value)**		
	183,788	**415,424**	**704,786**
Average velocity (m/s)	0.0474	0.0634	0.0601
Relative error (%)	−21.13	5.49	-

According to the geometric structure of the simulation model, a hydraulic experimental device was built at a scale of 1:1. The experimental device mainly includes a transparent side-blown furnace model built with acrylic plates, a high-speed camera, an air compressor, a pressure gauge, a flow meter, etc. A schematic diagram is shown in Figure 4.

In the experimental devices, the angle between the nozzle and the horizontal direction is 0°, the injection velocity is 29.44 m/s, the submerged depth at the center of the nozzle is 100 mm, and the flow rates of the nozzles on the left and right sides are equal. The same conditions as the experiments are used in the numerical simulation, and a schematic diagram of the results is shown in Figure 5. The distance between the bubble edge on the centerline of the nozzle and the side wall of the nozzle is taken as the gas penetration depth, as indicated by the labeled L in Figure 5.

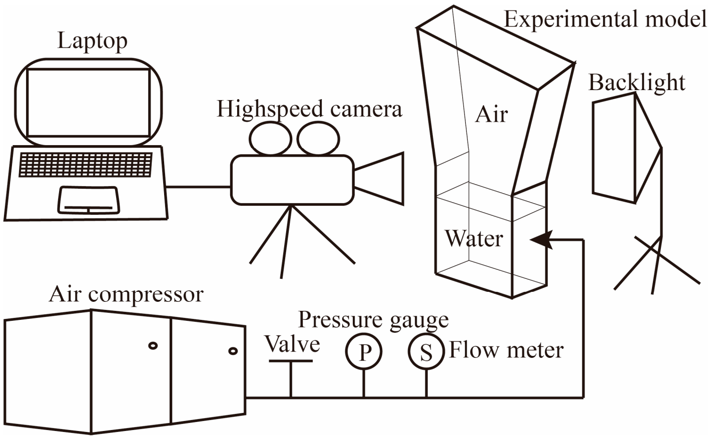

Figure 4. Schematic diagram of the experimental device.

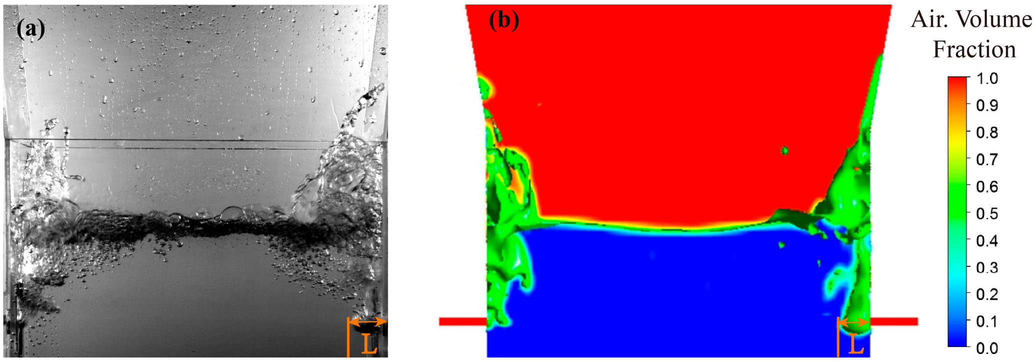

Figure 5. The schematic diagram of the results. (**a**) Experimental results; (**b**) simulation results.

As the gas is blowing into the model, periodic fluctuations occur in the process of change. To reduce the error, the statistical average over a period of 1 to 5 s was selected for analysis to verify the accuracy of the mathematical model. It can be found that the relative error between the simulation results and the experimental results is 5.16%, as shown in Table 2, indicating that the VOF model coupled with the realizable k-ε model is reliable in describing the behaviors of gas–liquid two-phase system motions in the scaled-down model.

Table 2. Experimental results and simulation results.

Physical Quantity	Experimental Value	Simulation Value
Average gas penetration depth (mm)	29.07	30.57
Relative error (%)	-	5.16

3. Results and Discussion

Selecting an injection velocity of 49.07 m/s, an injection angle of 0°, and a submerged depth of 100 mm as typical operating conditions, it can be found from the volume fraction equivalent surface diagram under typical working conditions (Figure 6) that the gas enters the model from the nozzle. Larger bubbles are formed near the nozzles first at 0.1 s; then, they move toward the model's center under the action of inertia. Concurrently, the gas velocity abates while the liquid velocity augments, resulting in an expansion in the gas–liquid interfacial area and an augmentation of the gas penetration depth. Subsequently, under the action of buoyancy, bubbles break through the liquid surface at 0.3 s, enter the gas-phase space, and drive the liquid upward beyond the original datum, with a continued increase in the gas–liquid interface area and liquid velocity, while the penetration depth begins to diminish. From 0.5 to 0.7 s, the liquid continues to be driven by the gas flow to splash upward, reaching the highest point at 0.7 s. Within this time frame, the area of the gas–liquid interface starts to reduce, the speed of the liquid decreases, and the penetration depth begins to increase once more as new gas flow gathers at the nozzle. Subsequently, the droplets fall under gravity into the liquid space at 0.8–0.9 s, and the gas–liquid interface area decreases, while the liquid velocity and penetration depth increase. The liquid continues to be driven by the gas, sputtering upward and then landing in a cyclic state, and the corresponding gas–liquid interface area, liquid velocity, and penetration depth also exhibit a cyclic state.

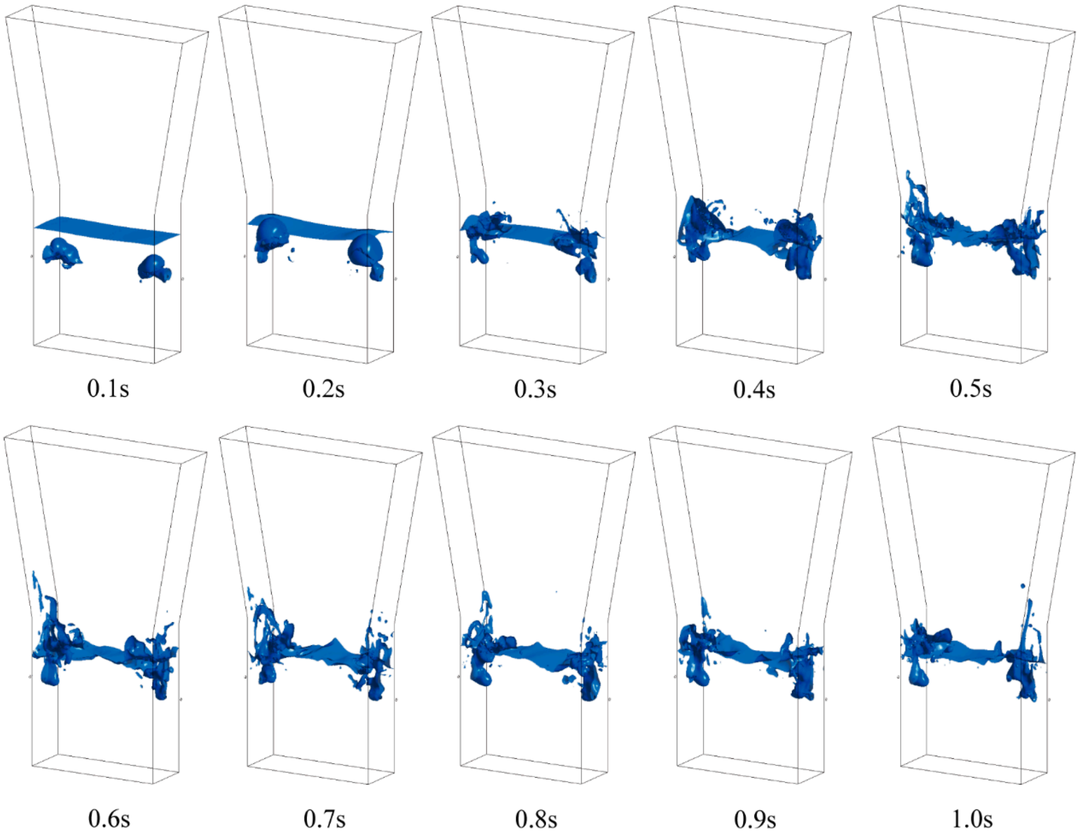

Figure 6. The equivalent surface at typical operating conditions.

3.1. Influence of Injection Velocity

To illustrate the effect of different gas injection velocities on the behavior of the gas–liquid two-phase system inside the furnace, four simulation cases with different injection velocities were established, and the parameters of the cases are shown in Table 3.

Table 3. Parameters for working conditions with different injection velocities.

Condition	Injection Velocity (m/s)	Injection Angle (°)	Submerged Depth (mm)
1	29.44	0	100
2	39.26	0	100
3	49.07	0	100
4	58.88	0	100

3.1.1. Changes in Interface Area at Various Injection Velocities

The gas–liquid interface area is obtained through the iso-surface of $\alpha_f = 0.5$. Figure 7 shows changes in the gas–liquid interface area at different injection velocities. The gas–liquid interface area rises quickly within 0.3 s and then starts to fluctuate. Combined with Figure 6, it can be found that the injection airflow in the model first forms small bubbles, which gradually become larger bubbles, and the area of the gas–liquid interface increases accordingly. At around 0.3 s, the bubbles break through the liquid surface and burst, which is the reason why the gas–liquid interface area increases and then falls back. As the fluid in the model shows a fluctuating cyclic reciprocal state after 1 s, the gas–liquid interface area also changes periodically. Under four different injection velocities, the higher the velocity, the larger the gas–liquid interface area, and the larger the maximum value of the gas–liquid interface area. When the injection velocity is relatively low, the amplitude of fluctuation in the gas–liquid interface area is smaller, and the frequency of change is faster. Conversely, when the inlet velocity is higher, the amplitude of fluctuation in the gas–liquid interface area is larger, while the frequency of change is lower.

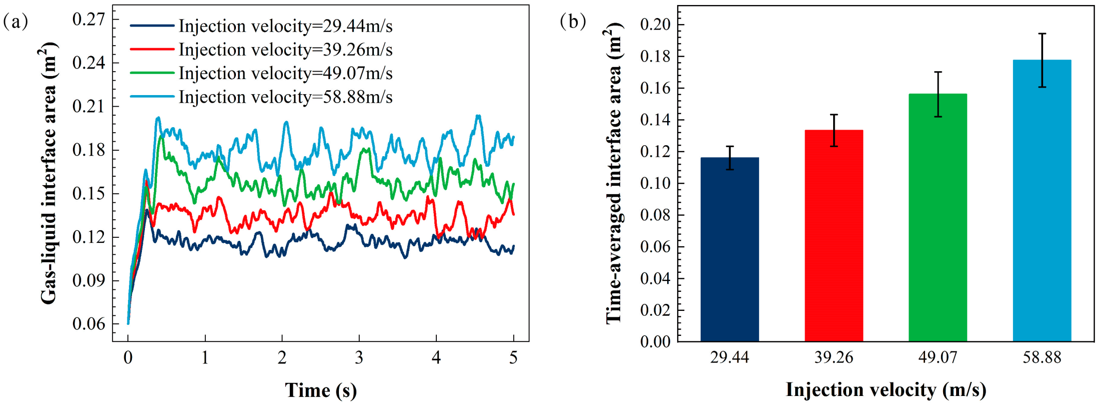

Figure 7. Gas–liquid interface area at different injection velocities: (**a**) curve of changes over time; (**b**) time-averaged area.

For the convenience of analysis, the statistical average of the data over a period of 1 to 5 s was taken as the object of study. The error bar displays the standard deviation of the gas–liquid interface area over time. A larger standard deviation indicates a more drastic change in the gas–liquid interface area over time. The average value of the interface area reached the maximum value of 0.1776 m^2 at an injection velocity of 58.88 m/s, which was 52.97% larger than that of 0.1161 m^2 at an injection velocity of 29.44 m/s. The larger the injection airflow velocity is, the greater the fluctuation amplitude of the corresponding gas–liquid interface area over time. Therefore, increasing the injection airflow velocity as much as possible can effectively enhance the interface area of gas–liquid contact in the furnace and, thus, promote the heat and mass transfer and chemical reaction processes between the gas and liquid phases.

3.1.2. Changes in Velocity and Turbulent Kinetic Energy at Various Injection Velocities

The volume-averaged velocity and turbulent kinetic energy of the liquid phase in the model were obtained every 0.1 s, and the curves of the two values at the typical injection angle and submerged depth with time were obtained and are shown in Figure 8. It can be found that the velocity of the liquid fluctuates periodically with time, and the general trend is that the higher the injection velocity, the higher the average velocity of the liquid. Due to varying injection velocities, the model exhibits discrepancies in the timing of bubble rupture, liquid splashing, and droplet fallback, resulting in inconsistent oscillation frequencies of the liquid velocity across different injection velocities. The injection airflow carries a considerable amount of momentum. When the airflow comes into contact with the liquid, the momentum of the airflow is transferred to the liquid through shearing action, driving the liquid into motion. The greater the velocity of the airflow, the larger the momentum transferred to the liquid, resulting in an increased ability to propel the liquid into motion.

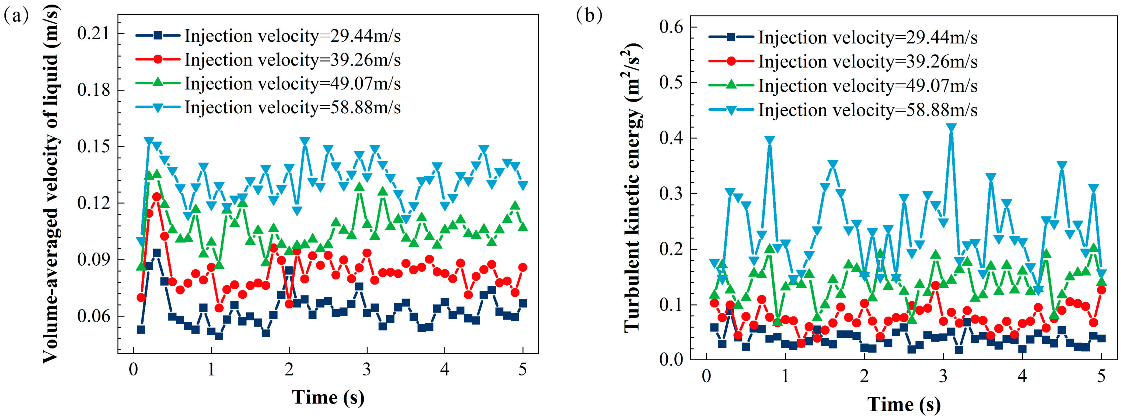

Figure 8. Variation in the velocity (**a**) and turbulent kinetic energy (**b**) of the liquid at different injection velocities.

The time-averaged velocity of liquid exhibited a maximum value of 0.13 m/s at an injection velocity of 58.88 m/s, representing a 116.67% increase compared to the value of 0.06 m/s observed at an injection velocity of 29.44 m/s. An increase in the injection airflow velocity generates stronger vortices and turbulence within the liquid. These vortices and turbulence effectively transfer energy from the airflow to the liquid, resulting in an increase in both the liquid's velocity and the amplitude of fluctuations.

Turbulent kinetic energy refers to the kinetic energy caused by the random, irregular flow of fluids, which is an important physical quantity for describing the characteristics of turbulence. It is defined as the root mean square of the fluctuating fluid velocity. It can be seen that the turbulent kinetic energy of the fluid also fluctuates up and down with time. Similarly, as the inlet velocity of the gas flow increases, the corresponding turbulent kinetic energy of the liquid also increases. Under the four working conditions, the frequencies of the fluctuations in turbulent kinetic energy are not consistent. The time-averaged values of the liquid's turbulent kinetic energy from 1 to 5 s are 0.04 m^2/s^2, 0.08 m^2/s^2, 0.14 m^2/s^2, and 0.24 m^2/s^2, respectively. The time-averaged turbulent kinetic energy at the maximum injection velocity increases by 500.00% compared to the value at the minimum injection velocity. This means that the magnitude of the increase in the liquid's turbulent kinetic energy is far greater than the proportion of the increase in the inlet gas flow velocity. Furthermore, the degree of fluctuation in the turbulent kinetic energy over a time period of 1 to 5 s also increases correspondingly.

Therefore, an increase in the injection airflow speed can effectively enhance the movement speed and turbulent kinetic energy of the fluid in the furnace. The results show that increasing the injection velocity from 29.44 to 58.88 m/s resulted in a 116.67% rise in liquid velocity and a 500.00% rise in liquid turbulent kinetic energy. This increases the amplitude of fluctuations in fluid velocity and turbulent kinetic energy. However, a higher injection airflow speed may also enhance the scouring effect on the furnace wall near the nozzle, so additional protection is needed in the vicinity of the nozzle area.

3.1.3. Changes in Gas Penetration Depth at Various Injection Velocities

As described above, the gas penetration depth is the distance between the edge of the bubble on the centerline of the nozzle and the side wall of the nozzle. When the gas is injected from the side nozzles, driven by its inertial force, it can rapidly penetrate the liquid surface and propagate toward the center of the model. During this initial stage, owing to the high velocity and focused jet, the gas can overcome the resistance of the liquid and penetrate deep into the liquid bulk. However, as the gas advances through the liquid, the interaction between the gas and liquid phases leads to energy transfer and dissipation, gradually converting the kinetic energy of the gas into the kinetic energy of the liquid. Consequently, the horizontal velocity of the gas diminishes rapidly, while the liquid velocity increases. Ultimately, when the horizontal kinetic energy of the gas is entirely dissipated, or when the gas begins to rise due to buoyancy forces, the maximum gas penetration depth is attained. According to Figure 9, the liquid fluctuates up and down under the action of airflow, making the penetration depth change with periodic fluctuations. The frequency of variation in the penetration depth is different under different incoming airflow velocities. The penetration depth is positively correlated with the incoming velocity.

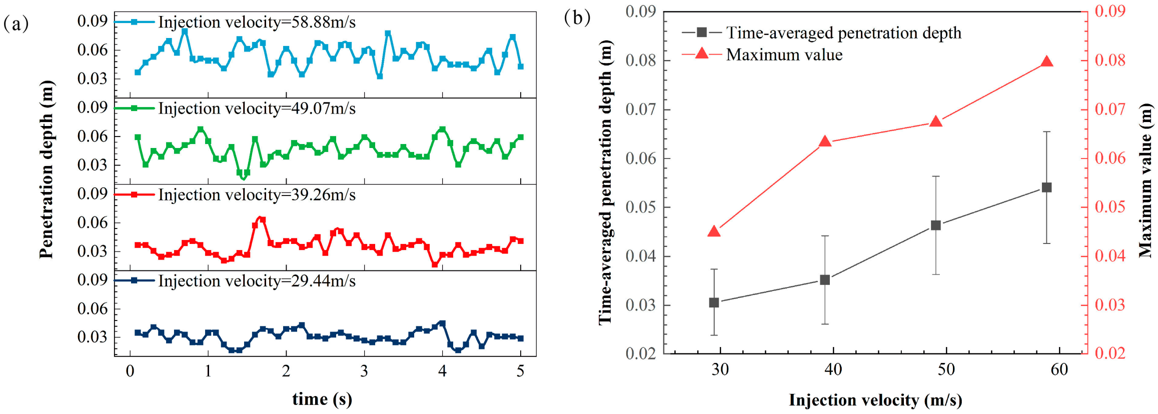

Figure 9. Gas penetration depth at different injection velocities: (**a**) curve of changes over time; (**b**) time-averaged penetration depth and the maximum value.

In the four operating conditions, the average penetration depths over a period of 1 to 5 s are 30.57 mm, 35.18 mm, 46.32 mm, and 54.08 mm respectively, which account for 7.64%, 8.80%, 11.58%, and 13.52% of the model width. The maximum value change in penetration depth is consistent with the time-averaged penetration depth change. When the injection velocity is 58.88 m/s, the maximum value is 79.59 mm, which is 19.90% of the model width. Therefore, increasing the injection airflow velocity can effectively enhance the penetration depth of the airflow in the liquid and promote the mixing efficiency of gas–liquid two-phase systems in the furnace.

Overall, it can be confirmed that increasing the injection velocity leads to an increase in the gas–liquid contact area, the liquid average velocity, the average turbulent kinetic energy, and the airflow penetration depth. Therefore, increasing the air injection velocity is considered an effective measure to enhance the momentum, heat, and mass transfer between the phases, thus effectively promoting the chemical reactions in the smelting bath.

3.2. Influence of Injection Angle

To illustrate the effects of different nozzle incidence angles on the behaviors of the gas and liquid phases in the model, three working conditions with different nozzle incidence angles are constructed. Meanwhile, considering the research content in Section 3.1, the nozzle injection velocity is set to 49.07 m/s. The specific working condition parameters are shown in Table 4.

Table 4. Parameters for working conditions with different injection angles.

Condition	Injection Velocity (m/s)	Injection Angle (°)	Submerged Depth (mm)
5	49.07	−30	100
6	49.07	0	100
7	49.07	30	100

3.2.1. Changes in Interface Area at Different Injection Angles

Figure 10 shows the change curve of the gas–liquid interface area with time at typical velocity and typical submerged depth. It can be found that the gas–liquid interface area rises sharply within 0.5 s and then falls back under three injection angles. The gas–liquid interface area shows a fluctuating cyclic state after 1 s of time. It can be observed that the gas–liquid interface area at an injection angle of −30° is significantly smaller than the values at injection angles of 0° and 30°. When examining the change in the gas–liquid interface area over time, it can be seen that, sometimes, the value is larger at an injection angle of 0°, while, at other times, the value is larger at an injection angle of 30°.

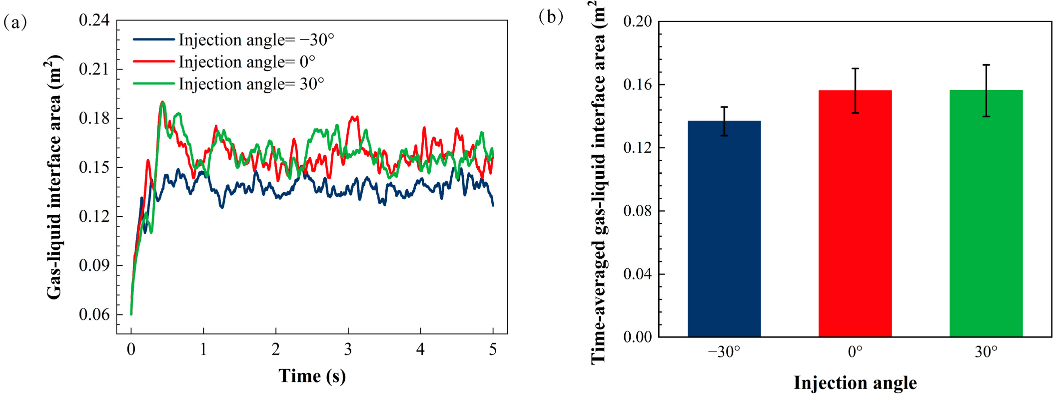

Figure 10. Gas–liquid interface area at different injection angles: (**a**) the curves of changes over time; (**b**) time-averaged area.

Under the three incidence angles, the difference between the time-averaged gas–liquid interface areas at 0° and 30° is not obvious, 0.1561 m^2 and 0.1562 m^2, respectively. The interface area at −30° is the smallest, 0.1368 m^2, which is about 88% of the former two incidence angles. From the analysis of the interface area of the gas–liquid two-phase interface alone, the worst effect of gas–liquid two-phase contact mixing in the furnace was observed at an incidence angle of −30°.

3.2.2. Changes in Velocity and Turbulent Kinetic Energy at Different Injection Angles

Similarly, it can be found that after the injection airflow moves upward and breaks through the liquid surface, the volume-averaged velocity of the liquid undergoes periodic fluctuations over time. The fluctuation frequencies of the liquid velocity over time are different under the three injection angles. When the injection angle is −30°, the liquid velocity is significantly smaller than the values when the injection angles are 0° and −30°, as shown in Figure 11.

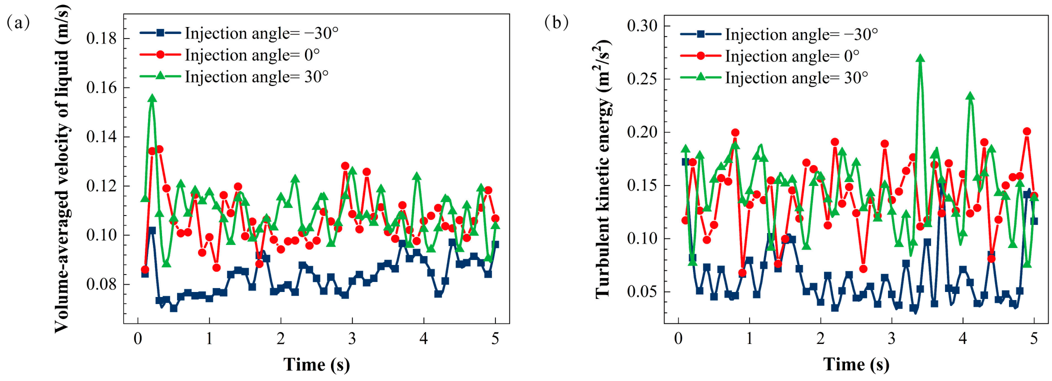

Figure 11. Variation in the velocity (**a**) and turbulent kinetic energy (**b**) of the liquid at different injection airflow angles.

When the injection angle is −30°, 0°, and 30°, the volume-averaged liquid velocity within 5 s is 0.08 m/s, 0.11 m/s, and 0.11 m/s, respectively. When the injection angle is 30°, the volume-averaged liquid velocity is marginally greater than the value observed when the injection angle is 0°. The fluctuation amplitude of the liquid velocity is larger when the injection angle is 0° and 30° compared to −30°. At an incidence angle of 30°, the airflow enters the liquid with a downward inclination, enabling a more efficient transfer of the airflow's momentum to the liquid in the region beneath the nozzle, thereby augmenting the liquid's velocity. Conversely, at a −30° injection angle, the airflow moves in an upward slant, leading to a relatively diminished contact area between the airflow and the liquid, which reduces the momentum transfer from the airflow to the liquid, and, consequently, the liquid velocity is lower.

The variation in the turbulent kinetic energy of the liquid exhibits a similar trend to that of the liquid velocity. The turbulent kinetic energy of the fluid also fluctuates up and down over time, with the fluctuation frequencies varying for the three injection angles. When the injection angle is −30°, the time-averaged turbulent kinetic energy of the liquid within a 5 s period is the smallest, and the value when the injection angle is 30° is slightly higher than the value when the injection angle is 0°. For an injection angle of 30°, the fluctuations in turbulent kinetic energy are more evident.

3.2.3. Changes in Gas Penetration Depth at Different Injection Angles

The penetration depth of the gas flow exhibits oscillatory behavior over time at three different injection angles, with varying frequencies of oscillation. At an injection angle of 30°, the gas flow trajectory is inclined obliquely downward. Subsequent to passing through the nozzle, the flow accumulates in the vicinity of the nozzle region due to inertial effects, continuing its oblique downward motion, before being redirected upward owing to the counteracting liquid resistance and buoyancy forces, resulting in a relatively larger penetration depth. Conversely, at an injection angle of −30°, the gas flow is inclined upward, and under the combined influence of inertial and buoyancy forces, it rapidly ascends, leading to a reduced penetration depth across the nozzle centerline. The mean penetration depths over a 5 s duration at injection angles of −30°, 0°, and 30° are 32.12, 46.32, and 60.53 mm, respectively, corresponding to 8.03%, 11.58%, and 15.13% of the model width. The maximum change in penetration depth is consistent with the time-averaged penetration depth change. When the injection angle is 30°, the maximum value is 97.96 mm, which is 24.49% of the model width, as illustrated in Figure 12.

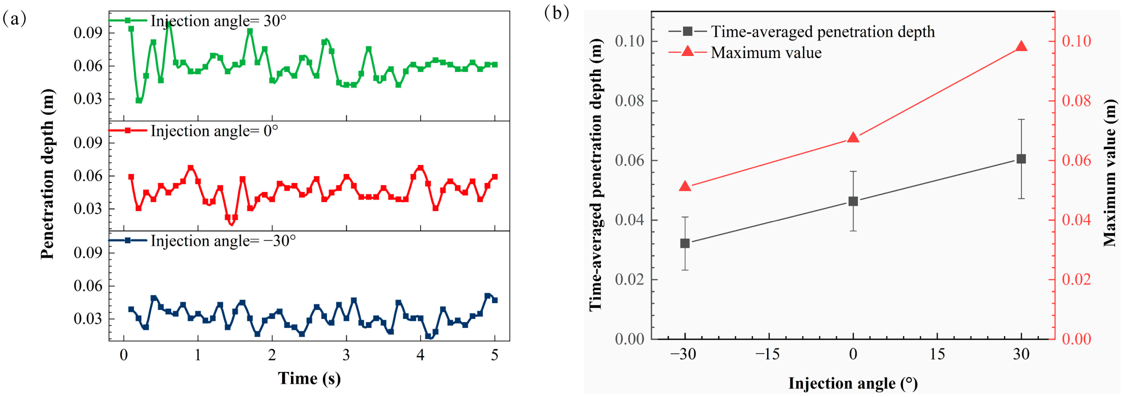

Figure 12. Gas penetration depth at different injection airflow angles: (**a**) curve of changes over time; (**b**) time-averaged penetration depth and the maximum value.

From the above analysis, it is clear that the incidence angles of airflow at 30° and 0° have created similar contact areas of gas–liquid, which are much larger than the result of −30°. Meanwhile, the largest values of evaluation indices are achieved at an incidence angle of 30°, including the liquid average velocity, turbulent kinetic energy, and the airflow penetration depth. Thus, the overall condition in the furnace is considered better when the injection angle is 30°.

3.3. Influence of Submerged Depth

To elucidate the influence of varying submerged depths on the behavior of the gas–liquid two-phase system within the model, this study establishes three operating conditions corresponding to three distinct submerged depths. Concurrently, in consideration of the research content presented in Sections 3.1 and 3.2, this section sets the nozzle injection velocity to 49.07 m/s and the nozzle injection angle to 0°. The specific parameters are delineated in Table 5.

Table 5. Parameters for working conditions with different submerged depths.

Condition	Injection Velocity (m/s)	Injection Angle (°)	Submerged Depth (mm)
8	49.07	0	50
9	49.07	0	100
10	49.07	0	150

3.3.1. Changes in Interface Area with Different Submerged Depths

Under typical velocity and injection angle conditions, the variation curves of the gas–liquid interface area with respect to time are illustrated in Figure 13. For all three submerged depth scenarios, the gas–liquid interface area rises sharply within 0.5 s, then declines and rises again, exhibiting a fluctuating cyclical state after 1 s. As the submerged depth increases, the gas flow travels a longer distance during its ascent, requiring more time to break through the liquid surface, consequently leading to an increase in the gas–liquid interface area. When the submerged depths are 50 mm, 100 mm, and 150 mm, the average interface areas over a period time of 1 to 5 s are 0.1108 m^2, 0.1561 m^2, and 0.1850 m^2, respectively. The greater the submerged depth, the larger the interface area and the greater the amplitude of fluctuations.

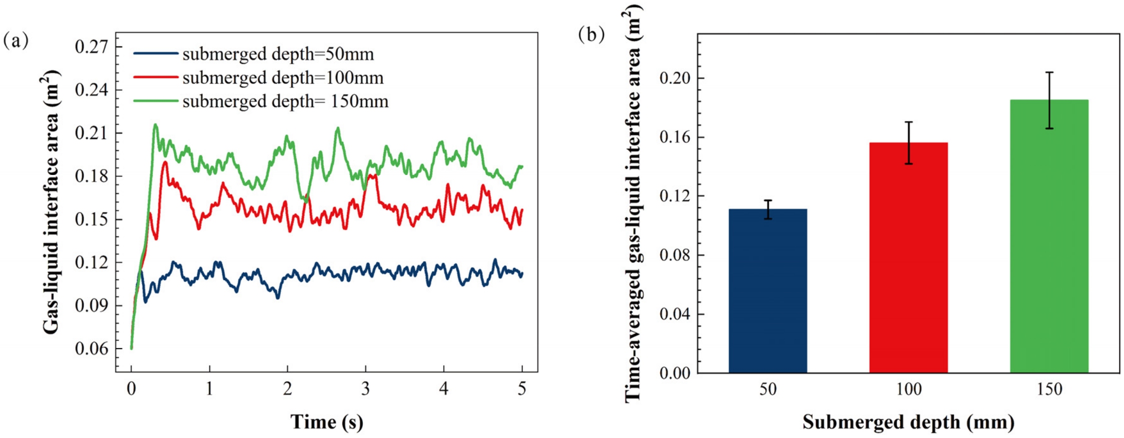

Figure 13. Gas–liquid interface area at different submerged depths: (**a**) curve of changes over time; (**b**) time-averaged area.

3.3.2. Changes in Velocity and Turbulent Kinetic Energy with Different Submerged Depths

As shown in Figure 14, under three different submerged depths, the liquid velocity exhibits periodic fluctuations in an upward and downward direction over time, with varying frequencies. Specifically, over a period time of 1 to 5 s, the average velocities at submerged depths of 50 mm, 100 mm, and 150 mm are 0.08 m/s, 0.11 m/s, and 0.12 m/s, respectively. The deeper the submerged depth, the greater the amount of liquid motion driven by the incoming airflow and, therefore, the greater the average velocity of the liquid.

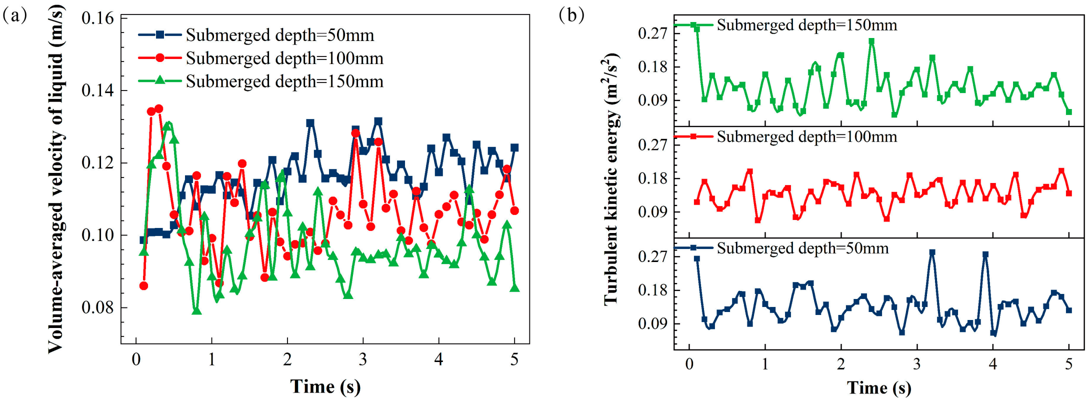

Figure 14. Variation in the velocity (**a**) and turbulent kinetic energy (**b**) of the liquid at different submerged depths.

Under three different submerged depths, the turbulent kinetic energy of the liquid fluctuates between 0.06 m^2/s^2 and 0.32 m^2/s^2 over time, and the frequency of change is also not consistent. Unlike the average velocity of the liquid, when the submerged depth is small, the average velocity of the liquid is relatively small, but the turbulent kinetic energy of the liquid is relatively large. This may be due to the fact that when the submerged depth is small, the mass of liquid above the nozzle is relatively small, and high-speed airflow enters the model, driving the liquid above the nozzle to move more violently, resulting in strong turbulent fluctuations. The liquid below the nozzle moves relatively smoothly, so the overall average velocity is relatively small. However, when the submerged depth is large, the mass of liquid above the nozzle is relatively large, and the momentum exchange between airflow and liquid is more thorough, but the turbulent fluctuations are weaker. The liquid below the nozzle moves relatively smoothly, so the overall average velocity is relatively large, but the turbulent kinetic energy is relatively small. The time-averaged values of liquid turbulent kinetic energy over a period time of 1 to 5 s for submerged depths of 50 mm, 100 mm, and 150 mm are 0.15 m^2/s^2, 0.14 m^2/s^2, and 0.12 m^2/s^2, respectively.

3.3.3. Changes in Gas Penetration Depth with Different Submerged Depths

At three different submerged depths, the penetration depth of airflow also exhibits oscillatory behavior over time, with different oscillation frequencies ranging from 22 mm to 78 mm. The average penetration depths corresponding to submerged depths of 50 mm, 100 mm, and 150 mm are 54.85 mm, 46.32 mm, and 53.67 mm, respectively, corresponding to 13.71%, 11.58%, and 13.42% of the model width. When the submerged depths are 50 mm and 150 mm, the maximum value of penetration depth is 77.55 mm, 19.39% of the model width, as shown in Figure 15.

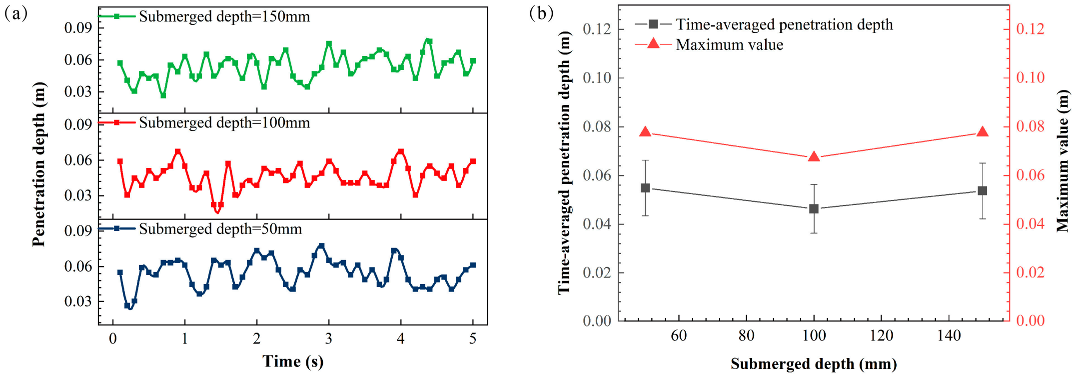

Figure 15. Gas penetration depth at different submerged depths: (**a**) curve of changes over time; (**b**) time-averaged penetration depth and the maximum value.

From the above analysis, it can be seen that, with an increase in the submerged depth, both the gas–liquid interface area and the liquid average velocity increase, but the turbulent kinetic energy decreases. The relationship between penetration depth and submerged depth needs further study. However, appropriately increasing the nozzle submerged depth can ensure the increase in the gas–liquid contact area, enhancing the momentum transfer ability between phases, thus promoting the reaction process.

4. Conclusions

The CFD modeling of the gas–liquid flow behaviors in a side-blown furnace was established. The numerical result was validated against the experiment, demonstrating good agreement. Then, the effects of injection velocity, angles, and nozzle's submerged depths were investigated. The main conclusions are shown as follows.

(1) The VOF model and the realizable k-ε model are proven to be reliable in simulating the gas–liquid two-phase flow in a side-blown furnace. The flow pattern can be summarized as follows. Initially, when the gas is injected, it forms a large bubble near the nozzle, pushing the liquid towards the bath center. Then, driven by buoyancy, the gas rises and breaks through the liquid surface, creating splashed droplets. Subsequently, as more gas enters, the liquid continues splashing, becoming a periodical pattern.

(2) The gas–liquid interface area, the liquid average velocity, the turbulent kinetic energy, and the airflow penetration depth are proportional to the airflow injection velocity. The results show that increasing the injection velocity from 29.44 to 58.88 m/s resulted in 52.97%, 116.67%, 500.00%, and 5.88% increases in the interface area, liquid velocity, liquid turbulent kinetic energy, and gas penetration depth, respectively. The increased injection velocity can effectively enhance the momentum exchange and reaction area between phases, thus promoting the smelting intensity.

(3) The overall condition in the furnace is better when the airflow injection angle reaches 30°, with the largest gas–liquid interface area, the gas penetration depth, the average velocity, and the average turbulence. However, these values are the smallest when the injection angle is $-30°$. Note that this study only analyzed the results under a certain injection velocity for different angles. Investigations on more velocities under different injection angles are suggested in the following studies.

(4) The relationship between the gas–liquid interface area and nozzle submerged depth is positively related. The liquid average velocity also increases with the rise of submerged depth. Thus, appropriately increasing the nozzle submerged depth in the furnace can enhance the gas–liquid contact area and promote series reactions.

Author Contributions: P.L.: data curation, writing—original draft preparation, software; Z.C.: conceptualization, methodology, supervision; Y.-P.S.: conceptualization, guidance. All authors have read and agreed to the published version of the manuscript.

Funding: This research received no external funding.

Data Availability Statement: The data that support the findings of this study are available from the corresponding author upon reasonable request.

Acknowledgments: We are grateful to the High Performance Computing Center of Central South University for assistance with the computations.

Conflicts of Interest: The authors declare no conflicts of interest.

References

1. Damle, C.; Sahai, Y. A criterion for water modeling of non-isothermal melt flows in continuous casting tundishes. *ISIJ Int.* **1996**, *36*, 681–689. [CrossRef]
2. Oryall, G.N.; Brimacombe, J.K. The physical behavior of a gas jet injected horizontally into liquid metal. *Metall. Trans. B* **1976**, *7*, 391–403. [CrossRef]
3. Ternstedt, P.; Tilliander, A.; Jönsson, P.G.; Iguchi, M. Mixing time in a side-blown converter. *ISIJ Int.* **2010**, *50*, 663–667. [CrossRef]
4. Wang, D.; Liu, Y.; Zhang, Z.; Zhang, Z.; Li, X. PIV measurements on physical models of bottom blown oxygen copper smelting furnace. *Can. Metall. Q.* **2017**, *56*, 221–231. [CrossRef]

5. Zhang, X.; Wu, J.; Zhang, H.; Ding, W.; Zhang, J. Visualization of Liquid Reaction in Submerged Top-blow Agitation Process. *Fuel Cells* **2021**, *21*, 18–23. [CrossRef]
6. Akashi, M.; Keplinger, O.; Shevchenko, N.; Anders, S.; Reuter, M.A.; Eckert, S. X-ray radioscopic visualization of bubbly flows injected through a top submerged lance into a liquid metal. *Metall. Trans. B* **2020**, *51*, 124–139. [CrossRef]
7. Song, K.; Jokilaakso, A. Transport phenomena in copper bath smelting and converting processes–A review of experimental and modeling studies. *Miner. Process. Extr. Metall. Rev.* **2022**, *43*, 107–121. [CrossRef]
8. Li, Z.; Wang, C.; Li, L.; Wu, J.; Yin, Z.; Tan, D. Numerical investigation of mesoscale multiphase mass transport mechanism in fibrous porous media. *Eng. Appl. Comput. Fluid Mech.* **2024**, *18*, 2363246. [CrossRef]
9. Li, L.; Xu, P.; Xu, W.; Wang, C.; Tan, D. Multi-field coupling vibration patterns of the multiphase sink vortex and distortion recognition method. *Mech. Syst. Signal Process.* **2024**, *219*, 111624. [CrossRef]
10. Chibwe, D.K.; Akdogan, G.; Aldrich, C.; Taskinen, P. Characterisation of phase distribution in a Peirce–Smith converter using water model experiments and numerical simulation. *Miner. Process. Extr. Metall.* **2011**, *120*, 162–171. [CrossRef]
11. Chibwe, D.K.; Akdogan, G.; Aldrich, C.; Taskinen, P. Modelling of mixing, mass transfer and phase distribution in a Peirce–Smith converter model. *Can. Metall. Q.* **2013**, *52*, 176–189. [CrossRef]
12. Valencia, A.; Rosales-Vera, M.; Orellana, C. Fluid dynamics in a teniente type copper converter model with one and two tuyeres. *Adv. Mech. Eng.* **2013**, *5*, 1–8. [CrossRef]
13. Zhang, H.L.; Zhou, C.Q.; Bing, W.U.; Chen, Y.M. Numerical simulation of multiphase flow in a Vanyukov furnace. *J. S. Afr. Inst. Min. Metall.* **2015**, *115*, 457–463. [CrossRef]
14. Liu, Y.T.; Yang, T.Z.; Chen, Z.; Zhu, Z.Y.; Zhang, L.; Huang, Q. Experiment and numerical simulation of two-phase flow in oxygen enriched side-blown furnace. *Trans. Nonferrous Met. Soc. China* **2020**, *30*, 249–258. [CrossRef]
15. Xiao, Y.; Lu, T.; Zhou, Y.; Su, Q.; Mu, L.; Wei, T.; Zhao, H.; Liu, F. Computational Fluid Dynamics Study on Enhanced Circulation Flow in a Side-Blown Copper Smelting Furnace. *JOM* **2021**, *73*, 2724–2732. [CrossRef]
16. Bian, Z.; Chen, D.; Sun, L.; Wang, L.; Zhao, H.; Zhen, Y.; Qi, T. Numerical Simulation and Optimization Analysis of Primary Air Injection Mode in Oxygen-Rich Side-Blown Bath Smelting Furnace. *J. Sustain. Metall.* **2023**, *9*, 871–883. [CrossRef]
17. Bian, Z.; Chen, D.; Sun, L.; Wang, L.; Zhao, H.; Zhen, Y.; Qi, T. Numerical Simulation and Experimental Investigation of Multiphase Flow in an Oxygen-Rich Side-Blown Bath Smelting Furnace. *JOM* **2023**, *75*, 3962–3974. [CrossRef]
18. Zou, Q.; Hu, J.; Yang, S.; Wang, H.; Deng, G. Investigation of the splashing characteristics of lead slag in side-blown bath melting process. *Energies* **2023**, *16*, 1007. [CrossRef]
19. ANSYS. *18.0 ANSYS Fluent Theory Guide 18.0*; Ansys Inc.: Canonsburg, PA, USA, 2017.